

Detecting gravitational wave bursts with LISA in the presence of instrumental glitches

Travis Robson and Neil J. Cornish

*eXtreme Gravity Institute, Department of Physics, Montana State University,
Bozeman, Montana 59717, USA*



(Received 18 November 2018; published 10 January 2019)

The Laser Interferometer Space Antenna (LISA) will open a rich discovery space in the millihertz gravitational wave band. In addition to the anticipated signals from many millions of binary systems, this band may contain new and previously unimagined sources for which we currently have no models. To detect unmodeled and unexpected signals we need to be able to separate them from instrumental noise artifacts, or glitches. Glitches are a regular feature in the data from ground-based laser interferometers, and they were also seen in data from the LISA Pathfinder mission. In contrast to the situation on the ground, we will not have the luxury of having multiple independent detectors to help separate unmodeled signals from glitches, and new techniques have to be developed. Here we show that unmodeled gravitational wave bursts can be detected with LISA by leveraging the different way in which instrument glitches and gravitational wave bursts imprint themselves in the time-delay interferometry data channels. We show that for signals with periods longer than the light travel time between the spacecraft, the “breathing mode” or Sagnac data combination is key to detection. Conversely, for short-period signals it is the time of arrival at each spacecraft that aids separation. We investigate the conditions under which we can distinguish the origin of signals and glitches consisting of a single sine-Gaussian wavelet and determine how well we can characterize the signal. We find that gravitational wave bursts can be unambiguously detected and characterized with just a single data channel (four functioning laser links), though the signal separation and parameter estimation improve significantly when all six laser links are operational.

DOI: [10.1103/PhysRevD.99.024019](https://doi.org/10.1103/PhysRevD.99.024019)

I. INTRODUCTION

Gravitational wave (GW) astronomy has tremendous potential for discovery, as has been spectacularly demonstrated by the ground-based LIGO/Virgo observatories [1,2]. The signals that have been detected to date have all been from binary systems, and are accurately modeled by theoretical templates. Going forward, it is hoped that entirely new classes of signals will be discovered, many of which we will not have templates for, either due to the difficulty in calculating the waveform (such as for supernovae), or from our ignorance about the existence of the source. Detecting signals of unknown morphology is challenging since the instruments themselves produce non-Gaussian transients, or glitches, that can be mistaken for signals of astrophysical origin.

The Laser Interferometer Space Antenna (LISA) [3], like its ground-based cousins, will very likely be afflicted by glitches. Glitches were seen in data from the LISA Pathfinder mission [4,5], and it is hard to imagine that they will be absent from the more complex LISA measurement system. Characterizing these glitches and accurately estimating their waveforms, will be an important component of the LISA global data analysis program.

Unlike the situation on the ground, where the availability of multiple independent interferometers simplifies the task of separating glitches from signals, with LISA we will have a single instrument. Nor will we have any “off-source” data, free of loud gravitational wave signals, with which to perform a measurement of the instrument noise. With LISA the signal and noise measurement must be done simultaneously [6] as part of a global analysis.

Similar concerns led to the developments of burst and glitch characterization analyses for LIGO. One such analysis was the wavelet-based Bayesian algorithm BayesWave [7]. This algorithm has played the key role for model-independent waveform reconstructions for most of the detected mergers seen by LIGO [1]. Its broad capabilities were best demonstrated when applied to the binary neutron star merger GW170817 [2]. BayesWave’s ability to characterize a loud instrumental glitch, obscuring a large fraction of the all-important late inspiral, allowed for an accurate reconstruction of the astrophysical signal with the glitch removed [8], so that other analyses could properly characterize the binary neutron star’s physical parameters [2]. For LISA, we wish to develop an algorithm to serve a similar purpose of analyzing glitches and bursts. Instrumental glitches in LISA studied here will fall into two categories: phasemeter and

acceleration. Optical path glitches reflect non-Gaussian deviations in the phasemeter length of any of LISA's six laser links. Acceleration glitches result from disturbances to the acceleration of LISA's test masses. Laser phase noise glitches will be neglected in this study since they will be suppressed in the time-delay interferometry (TDI) data channels [9]. Glitches can be represented through a superposition of sine-Gaussian wavelets in each component of the instrument. Gravitational wave bursts can similarly be represented by a superposition of wavelets. The signal is referenced to the Solar System barycenter (SSB) and then projected onto LISA by computing the instrument response. As a first step, we consider signals and glitches that are described by a single wavelet and defer the generalization to multiwavelet fits to future work.

To investigate our ability to characterize glitches and bursts consisting of a single wavelet, we will use Bayesian probability theory to calculate our degree of belief in the parameters which describe the injected signal, as quantified by the posterior distribution. The duration of these signals ranges from tens of seconds to roughly a day. Their duration, and frequency content in relation to the light travel time between the spacecraft will have important implications on our ability to characterize these signals and will also play a key role in our ability to distinguish whether the data contains a glitch (and which kind) or a burst. Glitches will enter the TDI data channels with time delays of the light travel time between spacecraft. This time is about 8.3 seconds for the nominal $L = 2.5$ Gm separation, which sets the LISA response transfer frequency $f_* = c/(2\pi L)$ to be 19.1 mHz. Wavelets with frequencies below the transfer frequency will be harder to characterize and distinguish. An additional piece of the puzzle are the data channels in which the wavelet's power crops up, and in what proportion. Acceleration glitches enter the data stream by afflicting two different phase measurements while phasemeter glitches afflict only one. Bursts, on the other hand, enter all phase measurements through time delays which depend on the various projected arm lengths depending on where the incident gravitational wave originates on the sky. While the power distribution is the most useful discriminant, the phasing becomes most important in the case of a malfunctioning LISA arm i.e., when we would be left with only one data channel. In this study we will address these considerations and investigate what we can learn and what features are most informative.

This work is organized as follows. Section II discusses the waveforms for phasemeter and acceleration glitches and for gravitational wave bursts. Section III reviews Bayesian inference and then describes the Markov chain Monte Carlo algorithm we employ to carry out the parameter estimation and model selection analyses in this paper. Section IV shows how well we can characterize glitch and burst parameters and recover the injected waveform. In Sec. V we explore under what conditions we are able to distinguish

between a glitch and a burst, and identify what features of the signal are most responsible for making the distinction. We end with a discussion of future work to be carried out in Sec. VI. Note that we work in units where $G = c = 1$.

II. GLITCH AND BURST MODELS

The LISA constellation consists of three spacecraft in the shape of a quasiequilateral triangle trailing behind Earth. The spacecraft have a total of six laser links, two for each arm. Each laser has its phase measured by phasemeters onboard the LISA spacecraft. A photon sent from the laser situated on spacecraft i , pointing towards spacecraft j , is emitted at time $t - L_{ij}$, where L_{ij} is the arm length connecting spacecraft i and j . The phase of this photon is measured at time t by the phasemeter on spacecraft j . This phase measurement can be approximated as [10]

$$\begin{aligned} \Phi_{ij}(t) = & C_i(t - L_{ij}) - C_j(t) + \psi_{ij}(t) + n_{ij}^o(t) \\ & - \hat{\mathbf{r}}_{ij}(t) \cdot (\mathbf{n}_{ji}^a(t - L_{ij}) - \mathbf{n}_{ij}^a(t)). \end{aligned} \quad (1)$$

The noise in the laser phase due to fluctuations of the laser frequency around its nominal value is described by the terms C_i . We refer to this noise as laser frequency noise. The term ψ_{ij} describes the phase shift induced by the presence of gravitational waves. The term n_{ij}^o represents the contribution from the optical bench on spacecraft j that receives light from spacecraft i . The last term represents the contribution to the phase measurement incurred by the acceleration noise of the test masses. Note that in this simplified model, where we are neglecting higher-order features of LISA's motion such as the flexing of the arms, the only component of the acceleration that is relevant is the differential acceleration along the line $\hat{\mathbf{r}}_{ij}$ connecting the center of mass of the two test masses.

These laser phase measurements are expected to be dominated by laser frequency noise. Current estimates indicate that the frequency fluctuation noise will be roughly 10 orders of magnitude greater than the changes in phase induced by the gravitational waves of interest [9]. The phase noise can be canceled using TDI. The TDI data combinations synthesize light paths of equal length by adding together phase measurements with time delays given by multiples of the instantaneous light travel times. This superposition cancels the laser frequency noise. When higher-order corrections to the spacecraft motion are taken into account the superposition of time-delayed phase measurements becomes more complicated. Here we use the simpler first-generation TDI data combinations. Three Michelson-like TDI channels can be formed from the signals extracted at each vertex of the observatory. These are denoted as X , Y , and Z . The X TDI channels is constructed as follows:

$$\begin{aligned}
X(t) = & \Phi_{12}(t-3L) - \Phi_{13}(t-3L) + \Phi_{21}(t-2L) \\
& - \Phi_{31}(t-2L) + \Phi_{13}(t-L) - \Phi_{12}(t-L) \\
& + \Phi_{31}(t) - \Phi_{21}(t), \tag{2}
\end{aligned}$$

where we have assumed that the LISA arm lengths are of constant length, i.e., $L_{ij}(t) = L$. The Y and Z channels are constructed through a cyclic permutation of the spacecraft labels, e.g., $1 \rightarrow 2$, $2 \rightarrow 3$, and $3 \rightarrow 1$ to construct the Y TDI channel. It is often convenient to work with the following linear combinations of the X , Y , Z channels:

$$A = \frac{1}{3}(2X - Y - Z), \tag{3a}$$

$$E = \frac{1}{\sqrt{3}}(Z - Y), \tag{3b}$$

$$T = \frac{1}{3}(X + Y + Z). \tag{3c}$$

Below the transfer frequency, the A and E channels synthesize two right-angle interferometers with a relative orientation of 45° , and provide instantaneous measures of the plus and cross polarization states of a gravitational wave. At these frequencies the T channel is mostly sensitive to the scalar breathing mode polarization state, which is absent in Einstein gravity,¹ and thus provides a null channel that is useful for measuring a particular combination of the noise contributions. When the noise levels are equal on each spacecraft, the cross-spectral density of the noise in the A , E , T channels vanishes [11,12].

An arbitrary signal seen in the TDI data channels may be reconstructed by a superposition of sine-Gaussian wavelets. In this study we use Gabor-Morlet wavelets. In the time-domain they are given by

$$\Psi = A e^{-(t-t_0)^2/\tau^2} \cos[2\pi f_0(t-t_0) + \phi_0], \tag{4}$$

where A is the wavelet amplitude, t_0 and f_0 are the central time and frequency, the wavelet time scale is τ —related to the wavelet quality factor Q through $\tau = Q/2\pi f_0$ —and ϕ_0 is the initial phase. Occasionally we will use the variable $\bar{\phi} = \phi_0 - 2\pi f_0 t_0$. The Fourier transform of the Gabor-Morlet wavelet is

$$\begin{aligned}
\tilde{\Psi} = & \frac{\sqrt{\pi}\tau A}{2} e^{-i(2\pi f t_0 + \phi_0)} \\
& \times [e^{-(\pi\tau(f+f_0))^2} + e^{2i\phi_0} e^{-(\pi\tau(f-f_0))^2}]. \tag{5}
\end{aligned}$$

¹Modified theories of gravity may predict a breathing mode for gravitational waves. It would be worthwhile to study the effect of this mode in the characterization of instrumental noise. We imagine that the distribution of power would be distinct enough to distinguish the origin of the signal when all laser links are functioning.

In the Fourier domain we see that in the large quality factor Q regime (or equivalently the large- τ regime) the second term in Eq. (5) is dominant. Ignoring the subdominant term, we can estimate the signal-to-noise ratio (SNR) in the case of white noise as

$$\begin{aligned}
\rho^2 \approx & \frac{4}{S_n(f_0)} \int_0^\infty \left(\frac{\sqrt{\pi}\tau A}{2} \right)^2 e^{-2(\pi\tau(f-f_0))^2} df \\
\approx & \sqrt{\frac{\pi}{2}} \frac{A^2 \tau}{S_n(f_0)}, \tag{6}
\end{aligned}$$

where $S_n(f_0)$ is an appropriate noise power spectral density which has been assumed constant such that we may approximate the integral. This result will become useful later when we wish to estimate a reasonable bandwidth in the frequency domain to calculate these signals over.

A. Instrumental glitches

To model instrumental glitches we inject a Gabor-Morlet wavelet into the appropriate term in Eq. (1). For example, a glitch in the phasemeter length pointing from spacecraft 1 to 2 is modeled as $\Phi_{12}(t) = n_{12}^0(t) = \Psi(t)$. We will label such a glitch as Φ_{12}^{pm} , where the superscript “pm” stands for phasemeter. Consider an acceleration glitch that is associated with the proof mass on spacecraft 2, referenced against spacecraft 1. Such a glitch will appear in two phase measurements: $\Phi_{12}(t) = -\Psi(t)$ and $\Phi_{21}(t) = \Psi(t-L)$. This acceleration glitch will be denoted as Φ_{12}^{as} . Laser phase glitches are neglected in this work since the TDI channels are constructed such that laser frequency noise is canceled.

The X , Y , and Z TDI channels can be constructed for both phasemeter and acceleration glitches analytically in the frequency domain. For the phasemeter glitch Φ_{12}^{pm} the response is

$$\tilde{X} = 2i\tilde{\Psi} e^{-2if/f_*} \sin \frac{f}{f_*}, \tag{7a}$$

$$\tilde{Y} = -2i\tilde{\Psi} e^{-if/f_*} \sin \frac{f}{f_*}, \tag{7b}$$

$$\tilde{Z} = 0. \tag{7c}$$

Note that there is no response in the Z channel. The factor of $\sin f/f_*$ is due to differencing the disturbance by the time delay. The only other phasemeter glitch that has no response in the Z channel is Φ_{21}^{pm} , which produces the response

$$\tilde{X} = 2i\tilde{\Psi} e^{-if/f_*} \sin \frac{f}{f_*}, \tag{8a}$$

$$\tilde{Y} = -2i\tilde{\Psi} e^{-2if/f_*} \sin \frac{f}{f_*}, \tag{8b}$$

$$\tilde{Z} = 0. \tag{8c}$$

TABLE I. This table contains the analytic first-generation TDI variables for phasemeter and acceleration glitches. Note that phasemeter glitches occupy two of the XYZ TDI channels while the acceleration glitches only occupy one. Acceleration glitches pick up an additional factor of the transfer function $\sin f/f_*$. A change in wavelet parameters, specifically the initial phase, leads to a perfect degeneracy between pairs of acceleration glitches when all three TDI channels are functioning. This is not the case for phasemeter glitches.

| | \tilde{X} | \tilde{Y} | \tilde{Z} |
|-------------------------|--------------------------------------------|--------------------------------------------|--------------------------------------------|
| Φ_{12}^{pm} | $2i\tilde{\Psi}e^{-2if/f_*} \sin(f/f_*)$ | $-2i\tilde{\Psi}e^{-if/f_*} \sin(f/f_*)$ | 0 |
| Φ_{21}^{pm} | $2i\tilde{\Psi}e^{-if/f_*} \sin(f/f_*)$ | $-2i\tilde{\Psi}e^{-2if/f_*} \sin(f/f_*)$ | 0 |
| Φ_{13}^{pm} | 0 | $2i\tilde{\Psi}e^{-if/f_*} \sin(f/f_*)$ | $-2i\tilde{\Psi}e^{-2if/f_*} \sin(f/f_*)$ |
| Φ_{31}^{pm} | 0 | $-2i\tilde{\Psi}e^{-if/f_*} \sin(f/f_*)$ | $2i\tilde{\Psi}e^{-2if/f_*} \sin(f/f_*)$ |
| Φ_{23}^{pm} | $2i\tilde{\Psi}e^{-if/f_*} \sin(f/f_*)$ | 0 | $-2i\tilde{\Psi}e^{-2if/f_*} \sin(f/f_*)$ |
| Φ_{32}^{pm} | $2i\tilde{\Psi}e^{-if/f_*} \sin(f/f_*)$ | 0 | $-2i\tilde{\Psi}e^{-2if/f_*} \sin(f/f_*)$ |
| Φ_{12}^{ac} | 0 | $4\tilde{\Psi}e^{-2if/f_*} \sin^2(f/f_*)$ | 0 |
| Φ_{21}^{ac} | $-4\tilde{\Psi}e^{-2if/f_*} \sin^2(f/f_*)$ | 0 | 0 |
| Φ_{13}^{ac} | 0 | 0 | $-4\tilde{\Psi}e^{-2if/f_*} \sin^2(f/f_*)$ |
| Φ_{31}^{ac} | $4\tilde{\Psi}e^{-2if/f_*} \sin^2(f/f_*)$ | 0 | 0 |
| Φ_{23}^{ac} | 0 | 0 | $4\tilde{\Psi}e^{-2if/f_*} \sin^2(f/f_*)$ |
| Φ_{32}^{ac} | 0 | $-4\tilde{\Psi}e^{-2if/f_*} \sin^2(f/f_*)$ | 0 |

We can already glean insight into how phasemeter glitches can be identified. When all six laser links are functioning, none of the phasemeter glitches can be made to look like the other. For example, suppose we try to match the X channel response of Φ_{12}^{pm} to that of Φ_{21}^{pm} . This would require a time shift of $t + L$ i.e., a factor of e^{if/f_*} in the frequency domain. This time shift will of course shift the Y response in the opposite desired direction in time. We cannot find a transformation of wavelet parameters such that any phasemeter glitch looks like another when all six laser links are functioning. If we are unfortunate enough to have only two functioning arms, we will be at a loss when attempting to distinguish these two glitches. That is if we have only the X channel, we will not be able to distinguish Φ_{12}^{pm} from a time-shifted Φ_{21}^{pm} .

We must also contend with acceleration glitches. The acceleration glitch Φ_{12}^{ac} has the TDI response

$$\tilde{Y} = 4\tilde{\Psi}e^{-2if/f_*} \sin^2 \frac{f}{f_*}, \quad (9)$$

where both the X and Z channels are null. All acceleration glitches have a response in only one of the X , Y , and Z data channels. Acceleration glitches also have an additional suppression from the transfer function $\sin f/f_*$. This is due to the acceleration glitch appearing in two phase measurements separated by the light travel time between spacecraft. With acceleration glitches however, we are unable to unambiguously determine their origin even when all six laser links are functioning. There are perfect degeneracies between pairs of acceleration glitches. For example, the response to the acceleration glitch Φ_{32}^{ac} ,

$$\tilde{Y} = -4\tilde{\Psi}e^{-2if/f_*} \sin^2 \frac{f}{f_*}, \quad (10)$$

has precisely the same form as Φ_{12}^{ac} except for a shift in its initial phase (by π). In the scenario where we lose one arm of the constellation we will be no worse off with respect to distinguishing acceleration glitches. The responses to glitches in other components are shown in Table I.

When generating these waveforms we wish to economically sample an appropriate bandwidth. The signal-to-noise ratio for a phasemeter glitch, given one data channel, can be estimated as

$$\rho_{\text{est}}^2 = \frac{\sqrt{\pi/2}A^2\tau}{S_{X,M}(f_0)}, \quad (11)$$

in the large- τ limit obtained from Eq. (6). $S_{X,M}$ is the Michelson-equivalent power spectral density defined as $S_{X,M} = S_X/4 \sin^2(f/f_*)$. Similarly, the SNR for an acceleration glitch can be estimated as

$$\rho_{\text{est}}^2 = \frac{4\sqrt{\pi/2}A^2\tau \sin^2(f_0/f_*)}{S_{X,M}(f_0)}. \quad (12)$$

A bandwidth of $\Delta f = 4(\rho_{\text{est}}/5)^2/\tau$ was used to capture in excess of 99.9% of the SNR in each glitch.

In addition to distributing power to different TDI channels, glitches in different components produce different phasings in the response. The phasing information depends critically on the frequency of the glitch, f_0 and the duration of the glitch τ . Higher-frequency glitches, in relation to LISA's transfer frequency, get heavily modulated by the transfer functions making it easier to determine their

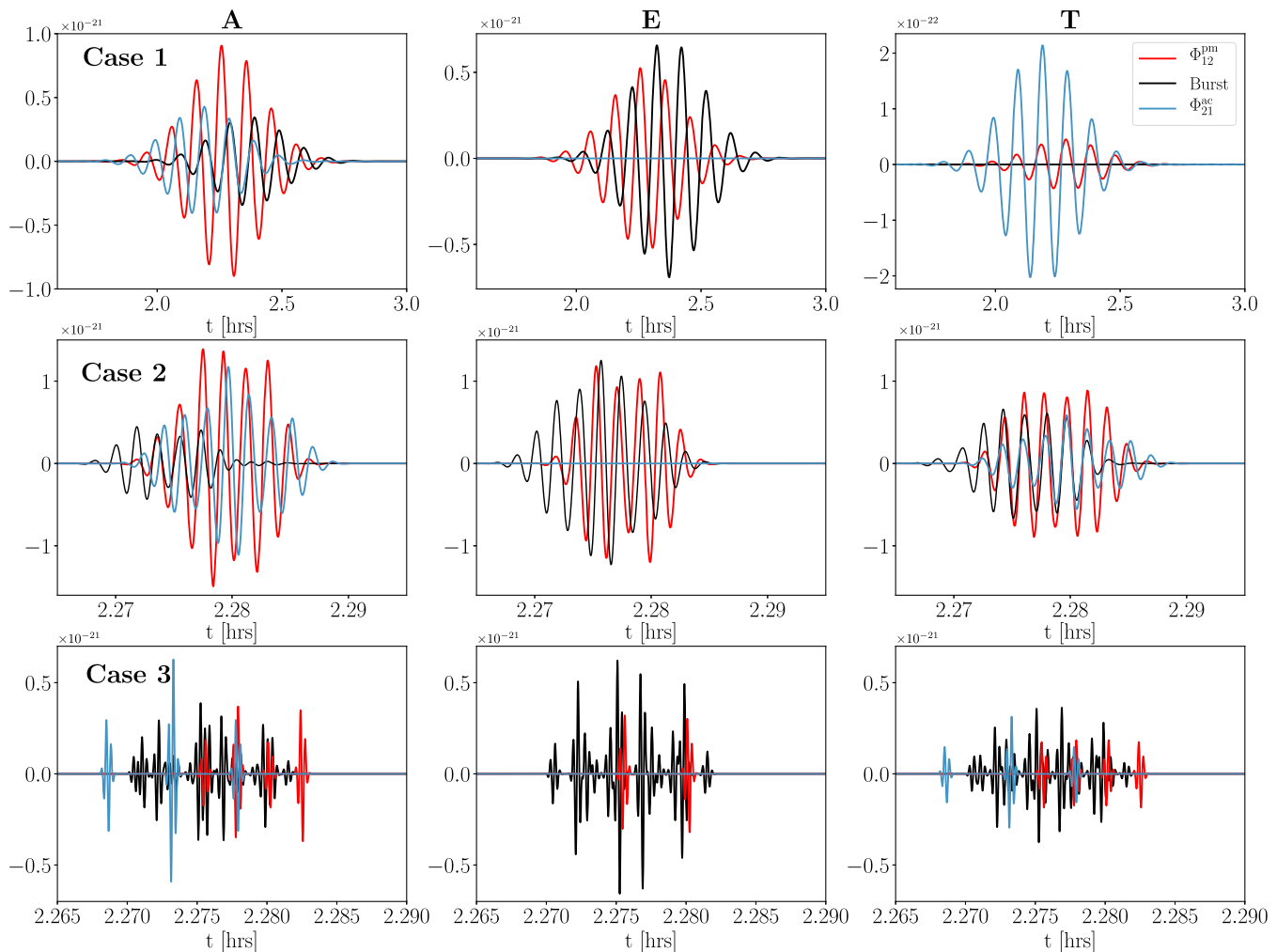


FIG. 1. This figure displays the A , E , and T TDI channel responses for various glitches (Φ_{12}^{pm} in red, and Φ_{21}^{ac} in blue) and gravitational wave bursts (in black). The top row shows wavelets with durations that are much longer than the light travel time between LISA spacecraft. The middle row shows wavelets with durations that are comparable to the light travel time. The bottom row shows wavelets with durations that are less than the light travel time, which leads to a clean separation of the glitch wavelets in the TDI channels. Note that the glitch wavelets only appear in a subset of the TDI channels.

origin. In Fig. 1 the A , E , and T TDI channels for phasometer glitches Φ_{12}^{pm} are displayed in red and acceleration glitches Φ_{21}^{ac} are shown in blue. The amplitudes of the optical and acceleration glitches were chosen for ease of comparison, while maintaining the correct relative amplitudes in the different TDI channels. The top row (case 1) displays glitches with the parameters $\tau = 0.2$ hours, and $f_0 = 2/\tau$ i.e., 2.7 mHz, placing this glitch well below the transfer frequency. These parameters give the glitch a quality factor of 12.6. Since the wavelet has a low frequency, its amplitude does not change substantially over the light travel time. This means that the construction of the TDI channels acts like a derivative of the input. In the middle row (case 2) the parameters of the wavelet are $\tau = L = 8.33$ seconds and $f_0 = 1.3/\tau = 156$ mHz ($Q \sim 8$). This wavelet has a temporal extent comparable to that of the light travel time between spacecraft. This results in a waveform that is the

superposition of two wavelets with a small time shift between them. Last, in the bottom row (cases 3) we see a wavelet of $\tau = 1$ second and $f_0 = 800$ mHz i.e., $Q = 5.1$. Here the frequency of the signal is substantially larger than the transfer frequency and the duration of the signal in time is much less than the light travel time, leading to a clean separation of the wavelets in the TDI channels. Note that in the low-frequency regime the phasometer glitch has a suppressed output in the T channel. We also see that the E channel response to the acceleration glitch is totally suppressed. This is because there is no Z or Y response for this specific acceleration glitch and the E channel has no X channel dependence.

B. Gravitational wave bursts

The phasometer length change due to a gravitational wave signal in the laser link connecting the i th and j th spacecraft is given by

$$\delta\ell_{ij}(t) = \mathbf{D}_{ij} : \int_{\xi_i}^{\xi_j} \mathbf{h}(t) dt, \quad (13)$$

where the colon denotes full contraction between the tensors, i.e., $\mathbf{A}:\mathbf{B} = A^{jk}B_{jk}$. The time t is SSB time, and $\xi_i = t_i - \hat{\mathbf{k}} \cdot \mathbf{x}_i$ is the wave variable defining surfaces of constant phase for the gravitational wave. The position of the i th spacecraft is \mathbf{x}_i , t_i is the time of emission of the laser photon from spacecraft i , and t_j is the time of reception of the laser photon at spacecraft j . The detector tensor \mathbf{D} is given by

$$\mathbf{D} = \frac{1}{2} \frac{\hat{\mathbf{r}}_{ij} \otimes \hat{\mathbf{r}}_{ij}}{1 - \hat{\mathbf{k}} \cdot \hat{\mathbf{r}}_{ij}}, \quad (14)$$

where $\hat{\mathbf{k}} = -(\sin\theta \cos\phi, \sin\theta \sin\phi, \cos\theta)$ is the gravitational wave propagation direction (θ and ϕ designate the source's position in spherical polar coordinates in the SSB frame). The quantity $\hat{\mathbf{r}}_{ij}$ is the unit-separation vector between the LISA spacecraft pointing from spacecraft i to spacecraft j . In this study the LISA orbits are kept to leading order in eccentricity thereby fixing the LISA arm length to be constant [10] $L = |\mathbf{r}_{ij}|$ for all i, j combinations.

The gravitational wave tensor \mathbf{h} is given by

$$\mathbf{h} = h_+(t)\mathbf{e}'_+(\psi, \theta, \phi) + h_\times(t)\mathbf{e}'_\times(\psi, \theta, \phi), \quad (15)$$

where $\mathbf{e}'_{+, \times}$ are the polarization tensors $\mathbf{e}_{+, \times}$ rotated by the polarization angle $\psi \in [0, \pi]$. In this work we assume that the gravitational waves are elliptically polarized such that, in the frequency domain, $\tilde{h}_\times = i\epsilon\tilde{h}_+$ is parametrized by the ellipticity $\epsilon \in [0, 1]$. We model the integrated gravitational wave polarizations as Gabor-Morlet wavelets such that $\int^t h_+(t') dt' = L\Psi(t)$. We may approximate the detector as static for the duration of a wavelet, since corrections would be on the order of $\tau/1$ yr. This means that we may safely evaluate all terms associated with the position of the detector at the central time of the wavelet t_0 and assume that the value is constant. The response to the wavelet in the frequency domain is then

$$\tilde{y}_{ij} = \frac{f}{f_*} (F_{ij}^{+'} + i\epsilon F_{ij}^{\times'}) \mathcal{T}_{ij}(f; \hat{\mathbf{k}}) \tilde{\Psi}(f) e^{-2\pi i f \hat{\mathbf{k}} \cdot \mathbf{x}_i(t_0)} \quad (16)$$

where $y_{ij} = \delta\ell_{ij}/2L$ and $F_{ij}^{+, \times} = [\hat{\mathbf{r}}_{ij} \otimes \hat{\mathbf{r}}_{ij}] : \mathbf{e}_{+, \times}$. \mathcal{T}_{ij} , the transfer function, is given by

$$\mathcal{T}_{ij} = \frac{1}{4} e^{i(\frac{f}{2f_*}(1 - \hat{\mathbf{k}} \cdot \hat{\mathbf{r}}_{ij}))} \text{sinc}\left(\frac{f}{2f_*}(1 - \hat{\mathbf{k}} \cdot \hat{\mathbf{r}}_{ij})\right). \quad (17)$$

The wavelet has its central time shifted by the light travel time between the SSB origin and spacecraft i through the phase factor $e^{2\pi i f \hat{\mathbf{k}} \cdot \mathbf{x}_i(t_0)}$ present in Eq. (16). The ellipticity ϵ and polarization angle ψ simply modulate the amplitude of

the response. We see that the sky angles modulate the amplitude too, but also enter into the phasing. As opposed to instrumental glitches, gravitational wave bursts will induce responses in all TDI channels. It is important to note though that for frequencies below the transfer frequency f_* , the gravitational wave response in the T channel is heavily suppressed [11]. This can be seen in the T channel response for case 1 in Fig. 1. The signal in each panel of Fig. 1 represents a gravitational wave burst. The sky angles are chosen such that $\cos\theta = 0.23$ and $\phi = 2.31$. The polarization angle is 0.45 and the ellipticity is 0.5. The wavelet parameters are precisely the same as those for the glitches in the panel the burst shares (give or take an amplitude factor or time shift for the sake of easy comparison). Note that for case 1 the signal response is distinctly different than for the glitch. Recall that the glitches in this case were cleanly separated. This is because glitches enter the data stream with time delays equal to the light travel time between spacecraft, which is longer than their extent in time. Gravitational waves enter the data stream with time delays equal to the projected arm lengths. This can lead to foreshortened arms allowing for some overlap between the wavelets as seen in case 3.

III. BAYESIAN INFERENCE

With the glitch and burst models established we now turn to the methods used to infer the properties of the gravitational wave signals and instrument glitches and develop probability distributions for the parameters of the models. These probabilities are quantified by the posterior distribution $p(\vec{\lambda}_{\mathcal{M}}|\mathbf{s}, \mathcal{M})$ which reflects our belief about a given set of parameters $\vec{\lambda}_{\mathcal{M}}$ which specify model \mathcal{M} given data \mathbf{s} . The posterior distribution is obtained via Bayes' theorem:

$$p(\vec{\lambda}_{\mathcal{M}}|\mathbf{s}, \mathcal{M}) = \frac{p(\mathbf{s}|\vec{\lambda}_{\mathcal{M}}, \mathcal{M})p(\vec{\lambda}_{\mathcal{M}}|\mathcal{M})}{p(\mathbf{s}|\mathcal{M})}, \quad (18)$$

where $p(\vec{\lambda}_{\mathcal{M}}|\mathcal{M})$ is the prior distribution for the parameters $\vec{\lambda}_{\mathcal{M}}$, $p(\mathbf{s}|\vec{\lambda}_{\mathcal{M}}, \mathcal{M})$ is the likelihood of the data given the parameters, and $p(\mathbf{s}|\mathcal{M})$ is the evidence for the model \mathcal{M} . Along with the assumptions we have already made in the construction of the TDI channels, we further assume that, aside from the glitches modeled here, the noise is stationary and Gaussian. The likelihood function for the data then takes the form

$$p(\mathbf{s}|\vec{\lambda}, \mathcal{M}) \propto \exp\left[-\frac{1}{2} \sum_I (\mathbf{s}_I - \mathbf{h}_I(\vec{\lambda})|\mathbf{s}_I - \mathbf{h}_I(\vec{\lambda}))\right], \quad (19)$$

where the subscript \mathcal{M} on the parameters has been dropped for simplicity. The sum is over TDI data streams $I = \{A, E, T\}$ (or just $I = \{X\}$ for some of our investigations). The noise-weighted inner product is defined as

$$(\mathbf{a}_I | \mathbf{b}_I) = 4\mathcal{R} \int_0^\infty \frac{\tilde{a}_I(f) \tilde{b}_I^*(f)}{S_{n,I}(f)} df. \quad (20)$$

The noise strain spectral densities in these data channels are given by

$$S_{AE} = \frac{16}{3} \sin^2 \frac{f}{f_*} \left[\left(2 + \cos \frac{f}{f_*} \right) P_{\text{OMS}} + 2 \left(3 + 2 \cos \frac{f}{f_*} + \cos \frac{2f}{f_*} \right) \frac{P_{\text{acc}}}{(2\pi f)^4} \right] \frac{1}{(2L)^2}, \quad (21a)$$

$$S_T = \frac{16}{3} \sin^2 \frac{f}{f_*} \left[\left(1 - \cos \frac{f}{f_*} \right) P_{\text{OMS}} + \left(3 - 4 \cos \frac{f}{f_*} + \cos \frac{2f}{f_*} \right) \frac{P_{\text{acc}}}{(2\pi f)^4} \right] \frac{1}{(2L)^2}, \quad (21b)$$

$$S_X = 4 \sin^2 \frac{f}{f_*} \left[4P_{\text{OMS}} + 8 \left(1 + \cos^2 \frac{f}{f_*} \right) \frac{P_{\text{acc}}}{(2\pi f)^4} \right] \frac{1}{(2L)^2}. \quad (21c)$$

The noise in the A and E channels, S_{AE} , is the same and the noise in the T channel is S_T . The single-link optical metrology noise power P_{OMS} and single test-mass acceleration noise power P_{acc} were quoted in Ref. [13]. Another contribution to the measured noise comes from millions of unresolved galactic binaries [14] emitting gravitational waves to which LISA is sensitive. Estimates of the unresolved galactic binary confusion noise for various observation periods can also be found in the same reference.

A. Maximization over nuisance parameters

In a fully Bayesian analysis we would compute the joint posterior distributions of all parameters in the model. To simplify the analysis and achieve more rapid convergence, we chose to eliminate certain nuisance parameters by analytically maximizing the likelihood with respect to these parameters using the \mathcal{F} -statistic approach (we could have analytically *marginalized* over the nuisance parameters instead [15], but it is much faster and simpler to maximize). The \mathcal{F} -statistic [16] provides a way to maximize the likelihood over the extrinsic parameters: A , ϕ_0 for a glitch, and A , ϕ_0 , ψ , ϵ for a burst. Through the use of several filters, constructed from the burst or glitch wavelet with specific choices of extrinsic parameters, one may construct the maximized likelihood. To understand how to construct the \mathcal{F} -statistic it is useful to consider the burst model in the large- τ and low-frequency limit

$$y_{ij} = -\frac{f_0}{4f_*} [F_{ij}^{+'} \sin(2\pi f_0 t_i + \bar{\phi}) + \epsilon F_{ij}^{\times'} \cos(2\pi f_0 t_i + \bar{\phi})], \quad (22)$$

where $t_i = t - \hat{\mathbf{k}} \cdot \mathbf{x}_i$. This signal may be deconstructed into four terms which consist of a constant amplitude dependent on extrinsic parameters multiplying a time-dependent factor, additionally dependent on the intrinsic parameters (f_0 , τ , t_0 , θ , ϕ)

$$y_{ij} = \sum_k a_k A^k(t). \quad (23)$$

The four filters $A^k(t)$

$$A^1 = -\frac{f_0}{4f_*} F_{ij}^{+'} \sin(2\pi f_0 t_i), \quad (24a)$$

$$A^2 = -\frac{f_0}{4f_*} F_{ij}^{\times'} \sin(2\pi f_0 t_i), \quad (24b)$$

$$A^3 = -\frac{f_0}{4f_*} F_{ij}^{+'} \cos(2\pi f_0 t_i), \quad (24c)$$

$$A^4 = -\frac{f_0}{4f_*} F_{ij}^{\times'} \cos(2\pi f_0 t_i) \quad (24d)$$

may be constructed by inserting the extrinsic parameters listed in Table II into the burst waveform generator. The glitch \mathcal{F} -statistic filters can be constructed by the parameter choices (1) $A = 1$, $\bar{\phi} = 0$ and (2) $A = 1$, $\bar{\phi} = -\pi/4$. The extrinsic parameter coefficients are

$$a_1 = A(\cos 2\psi \cos \bar{\phi} - \epsilon \sin 2\psi \sin \bar{\phi}), \quad (25a)$$

$$a_2 = A(-\sin 2\psi \cos \bar{\phi} - \epsilon \cos 2\psi \sin \bar{\phi}), \quad (25b)$$

$$a_3 = A(\cos 2\psi \sin \bar{\phi} + \epsilon \sin 2\psi \cos \bar{\phi}), \quad (25c)$$

$$a_4 = A(-\sin 2\psi \sin \bar{\phi} + \epsilon \cos 2\psi \cos \bar{\phi}). \quad (25d)$$

The noise-weighted inner product of these filters with the data $N^k = (\mathbf{s} | \mathbf{A}^k)$ can be used to construct the maximized relative likelihood

$$\mathcal{F} = \log \mathcal{L} = \frac{1}{2} (M^{-1})_{mn} N^m N^n. \quad (26)$$

TABLE II. Plugging these parameters into the gravitational wave burst waveform generator will construct the filters (24a)–(24d). The resulting filters can then be used to maximize the likelihood over the extrinsic parameters.

| Filter | A | $\bar{\phi}$ | ψ | ϵ |
|--------|-----|--------------|----------|------------|
| A^1 | 1 | 0 | 0 | 0 |
| A^1 | 1 | 0 | $-\pi/4$ | 0 |
| A^3 | 1 | $\pi/2$ | 0 | 0 |
| A^4 | 1 | $\pi/2$ | $-\pi/4$ | 0 |

The value \mathcal{L} is the relative likelihood, i.e., the ratio between the likelihood assuming \mathbf{h} contains a burst and the likelihood assuming there is no such signal, i.e., $\mathbf{h} = 0$, such that

$$\log \mathcal{L} = (\mathbf{s}|\mathbf{h}) - \frac{1}{2}(\mathbf{h}|\mathbf{h}). \quad (27)$$

The results hold for summing over multiple data channels such as when we use the A , E , and T TDI channels. The matrix $M^{mn} = (\mathbf{A}^m|\mathbf{A}^n)$ is simply the inner product matrix of the filters. Although, in this study we do not make use of the extrinsic parameters which maximize the likelihood it may prove useful in a future study to be able to calculate them. Inverting the equations for the filter returns the extremized extrinsic parameters

$$A = \sqrt{\frac{1}{2}(s + \sqrt{pq})}, \quad (28a)$$

$$\epsilon = \frac{s - \sqrt{pq}}{2(a_1 a_4 - a_2 a_3)}, \quad (28b)$$

$$\tan(2\psi) = \frac{a_1^3 + 2a_2 a_3 a_4 + a_1(a_2^2 + a_3^2 - a_4^2 + \sqrt{pq})}{a_1^2 a_2 + 2a_1 a_3 a_4 + a_2(a_2^2 - a_3^2 + a_4^2 + \sqrt{pq})}, \quad (28c)$$

$$\tan \bar{\phi} = \frac{a_1^2 + a_2^2 - a_3^2 - a_4^2 + \sqrt{pq}}{-2(a_1 a_3 + a_2 a_4)}, \quad (28d)$$

where $s = a_1^2 + a_2^2 + a_3^2 + a_4^2$, $p = (a_2 + a_3)^2 + (a_1 - a_4)^2$, and $q = (a_2 - a_3)^2 + (a_1 + a_4)^2$. For glitches the amplitude and phase can be extracted via

$$A = \sqrt{a_1^2 - a_2^2}, \quad (29a)$$

$$\tan \bar{\phi} = \frac{-a_2}{a_1}. \quad (29b)$$

B. Markov chain Monte Carlo

In this study we wish to characterize what we can learn about a wavelet present in the data. To accomplish this we marginalize the posterior distribution via the Markov chain Monte Carlo (MCMC) algorithm. Suppose we inject a signal into our data \mathbf{s} . Upon choosing a model specified by the initial set of parameters \vec{x} we generate a proposed set of parameters from a probability density $q(\vec{y}|\vec{x})$. The chance that we accept this new set of parameters \vec{y} is given by the Hastings ratio

$$H = \min \left\{ 1, \frac{p(\mathbf{s}|\vec{y}, \mathcal{M})p(\vec{y}|\mathcal{M})q(\vec{x}|\vec{y})}{p(\mathbf{s}|\vec{x}, \mathcal{M})p(\vec{x}|\mathcal{M})q(\vec{y}|\vec{x})} \right\}. \quad (30)$$

The sequence of parameters we accept, called a chain, constitute samples from the posterior distribution $p(\vec{\lambda}_{\mathcal{M}}|\mathbf{s}, \mathcal{M})$. The MCMC we created uses the \mathcal{F} -statistic likelihood, extremizing the likelihood over the extrinsic parameters of the signal. This effectively reduces the search space of the MCMC, greatly improving its convergence, especially for the burst model which otherwise converges slowly when the sky location is poorly-constrained.

For the MCMC developed in this study uniform priors were set for the parameter set $\{\log A, f_0, t_0, \log \tau, \bar{\phi}, \cos \theta, \phi, \psi, \epsilon\}$. To aid in the convergence of the MCMC we used a mixture of proposal distributions. We utilized local Gaussian approximations to the posteriors through the Fisher matrix (which approximates the inverse covariance matrix)

$$\Gamma_{ij} = \sum_{\mathbf{I}} (\mathbf{h}_{\mathbf{I},i}|\mathbf{h}_{\mathbf{I},j}), \quad (31)$$

where $\mathbf{h}_{\mathbf{I},i}$ represent the derivative of the waveform (in the \mathbf{I} th data channel) with respect to the i th parameter λ_i . These derivatives were calculated numerically using finite differencing of the waveforms discussed in Sec. II. We occasionally used proposals from the prior distribution. Since we are not currently developing a detection algorithm, only an MCMC which characterizes the signal, we used a targeting distribution to help the MCMC find appropriate central frequencies f_0 and decay factor τ . For f_0 and τ individually, this proposal consisted of a Gaussian distribution centered on the true parameter used to generate the injection. The width of the Gaussian was chosen based on the Fisher matrix estimation for the error in that parameter. To improve the acceptance rate of this proposal distribution the Gaussian was mixed with a 20% by weight uniform distribution covering the prior range. Differential evolution [17] proposals were also used. Last, a time-shift proposal was used to help highly oscillatory wavelets where shifts, forwards or backwards, in the central time of the wavelet by the wavelet's period were proposed (with an appropriate shift in initial phase).

To further improve convergence, and to ensure a thorough exploration of parameter space—such as investigating the existence of secondary modes on the sky for bursts—parallel tempering [18] is utilized. During parallel tempering multiple chains are simulated simultaneously at different temperatures, i.e., their likelihoods are flattened $p(\mathbf{s}|\vec{\lambda}, \mathcal{M})^{\beta_j}$, where $\beta_j = 1/T_j$ is the inverse temperature for the j th chain. The cold chain, i.e., $T_0 = 1$, represents samples from the posterior distribution. The chains at various temperatures propose and accept new parameters just as before, but with the flattened likelihood. Occasionally, parameter swaps between chains neighboring in temperature are proposed based on the probability

$$H_{\text{PT}} = \min \left\{ 1, \frac{p(\mathbf{s}|\vec{\lambda}_j, \mathcal{M})^{\beta_{j+1}} p(\mathbf{s}|\vec{\lambda}_{j+1}, \mathcal{M})^{\beta_j}}{p(\mathbf{s}|\vec{\lambda}_j, \mathcal{M})^{\beta_j} p(\mathbf{s}|\vec{\lambda}_{j+1}, \mathcal{M})^{\beta_{j+1}}} \right\}. \quad (32)$$

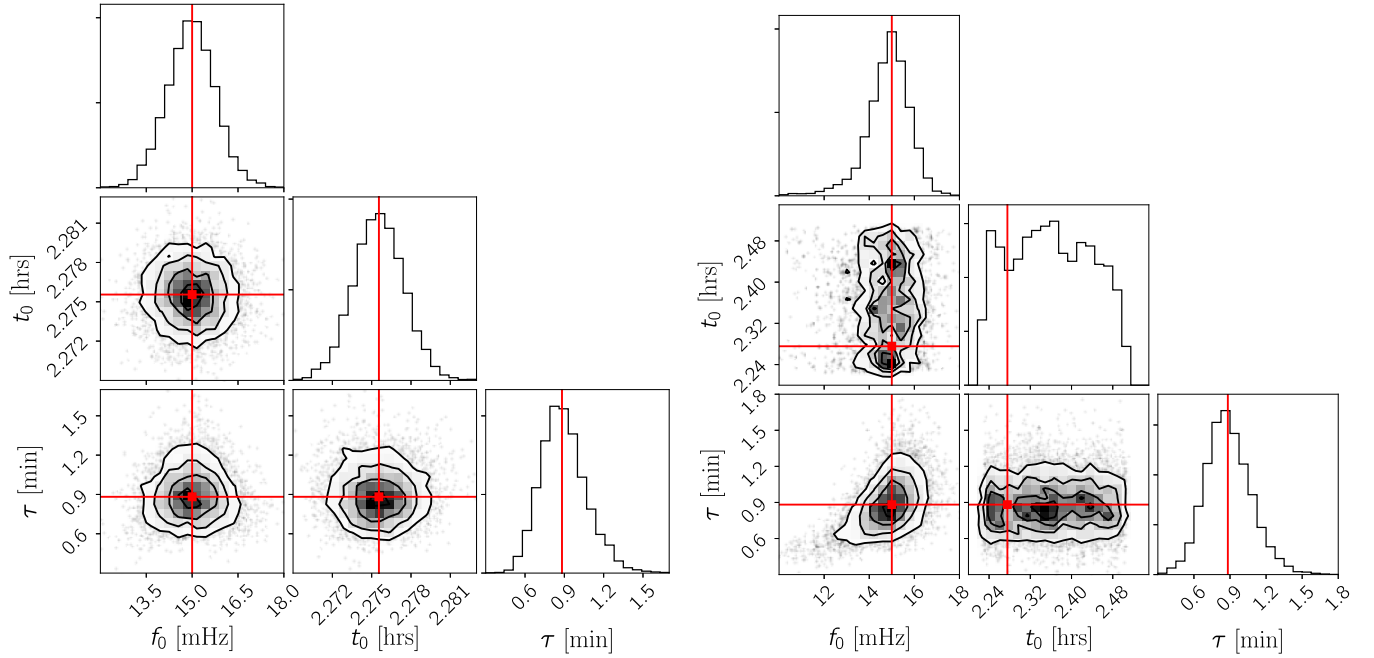


FIG. 2. Marginalized posteriors for the parameters f_0 , t_0 , and τ are displayed for a phasemeter glitch Φ_{12}^{pm} in the left panel and a gravitational wave burst in the right panel. The fully marginalized posteriors for f_0 and τ are similar for the two injections (while the joint posterior exhibits some correlation for the burst), but the central time posteriors differ significantly. The injected parameters are marked by the red lines.

Parallel tempering vastly improves convergence once a proper selection of temperatures is made. The maximum temperature is chosen such that the hottest chain freely explores the parameters' prior volume, while not so hot as to be redundant in the prior space exploration as cooler chains. In Sec. VA we see how parallel tempering additionally aids us in determining whether a glitch (and which one) or a burst best explains the data.

IV. PARAMETER ESTIMATION

The MCMC may now be used to address questions such as how well we can characterize the parameters of the signal and recover the waveform itself. The central frequency f_0 and time damping factor τ are typically well determined for bursts and glitches. An example marginalized posterior for these parameters is seen in Fig. 2. The left panel shows marginalized posterior distributions for a phasemeter glitch Φ_{12}^{pm} and the right panel shows marginalized posteriors for the same parameters for a burst. The injected signals both have an SNR of 8. The SNR is given by

$$\rho = \sum_I (h_I | h_I). \quad (33)$$

They share the parameter values $f_0 = 15$ mHz, $t_0 = 0.5T$ (where T is the observation period), and $\tau = 53$ seconds (giving the wavelets a quality factor of 5.0). The burst injection has the following additional parameters:

$\cos\theta = 0.23$, $\phi = 2.31$, $\psi = 0.45$, and $\epsilon = 0.5$. We see that the fully marginalized posterior distributions for the central frequency f_0 and τ are rather similar for these two injections. However, the posteriors for the central time t_0 are quite distinct in a significant way. One can show through a simple Fisher matrix calculation for a wavelet [7] that the standard deviation in t_0 for a wavelet scales as $1/\rho\tau$. The injected glitch has a measured standard deviation of 53 seconds while the Fisher matrix standard deviation estimates an error of 70 seconds, demonstrating agreement. The standard deviation in t_0 for the burst is 4.6 minutes, which is much larger than that of the glitch which must be attributed to the more complex response of a burst compared to a glitch.

The reason for the increase in error associated with the central time of the burst can be seen in Fig. 3. There exists a substantial correlation between the azimuthal sky angle ϕ and t_0 . If we do not appropriately constrain the central time it turns out that we cannot determine the sky location, which is the case for this example burst. We can understand this by looking at the low-frequency response to a GW burst signal. In this regime, the Michelson-equivalent A and E TDI channels are proportional to $\frac{f}{f_*} \tilde{\Psi} e^{-2\pi i f \mathbf{k} \cdot \mathbf{x}_1}$ modulo overall constants that differ between the channels. The T channel is null in this limit. We see that the sky angles enter the phasing through a time shift factor multiplying the Fourier transform of the Gabor-Morlet wavelet. Since this factor is a time shift, the sky angles are almost perfectly degenerate with the central time of the wavelet. The

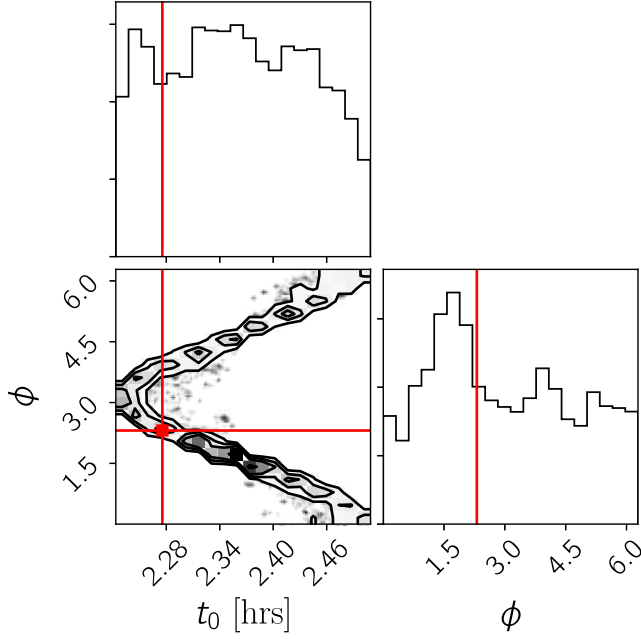


FIG. 3. The joint posterior for the azimuthal angle ϕ and the wavelet's central time t_0 as well as their fully marginalized posteriors. The injected parameters are again marked by the red lines. There exists a very large correlation between these two parameters.

likelihood is approximately constant under mappings of the azimuthal sky location and central time that keep the combination $t_0 - R \sin \theta \cos(2\pi f_m t_0 - \phi)$ fixed, where $f_m = 1/\text{yr}$ is the orbital modulation frequency and $R = 1 \text{ AU}$. This relationship holds to leading order in the orbital eccentricity. Higher-order corrections to the phasing incorporate additional information about the sky location in the form of the projected arm lengths $L_{ij} = L(1 - \hat{\mathbf{k}} \cdot \hat{\mathbf{r}}_{ij})$.

In Fig. 4 we see the posterior distribution for the projected arm lengths from a burst injection of the same sky location, polarization, ellipticity, and SNR as in the previous example, but now the central frequency is 50 mHz and $\tau = 16$ seconds. This shorter envelope allows the central time to be measured and therefore the sky location to be better determined. The duration of the wavelet is more important in determining the sky location than the central frequency.

In Fig. 5 we see the posterior distribution for the sky location for two different high-frequency bursts. Both bursts in Fig. 5 have the same sky location, which is denoted by the blue dot in the sky map on the left. The central frequency of each source is 50 mHz. The duration of the source shown on the left is $\tau = 16$ seconds (i.e., the same burst used in Fig. 4) while the sky map on the right is for a source with $\tau = 2.8$ minutes. We see that the origin of the burst on the sky has been localized for the short-duration burst. This is due to the tight constraint on the central time of the wavelet. When the

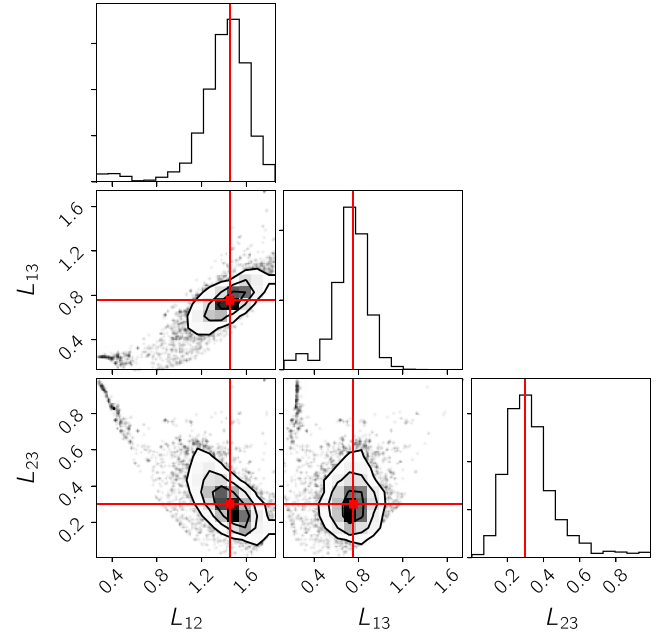


FIG. 4. The posterior distributions for the quantities $1 - \hat{\mathbf{k}} \cdot \hat{\mathbf{r}}_{ij}$ are displayed here, i.e., LISA's projected arm lengths for a high-frequency gravitational wave burst, normalized by the arm length $L = 2.5 \text{ Gm}$. The red lines indicate the injected values for the GW burst signal.

central time of the wavelet is measured to better than the light travel time between spacecraft we begin to have the power to localize the wavelet on the sky. The source shown on the right has a longer duration and poorer constraint on the central time, and therefore a poorer constraint on the sky location. An interesting structure emerges on the sky posterior for the right source. The most important factors in determining the sky location are the measured values for the projected arm lengths. The projected arm lengths can be related to the sky locations via the relations

$$\begin{aligned} \hat{\mathbf{k}} \cdot \hat{\mathbf{r}}_{12}(t) = & -\frac{1}{2} \cos \theta \left[\cos \alpha + \cos \left(\alpha + \frac{\pi}{3} \right) \right] \\ & + \frac{1}{8\sqrt{3}} \sin \theta \left[2 \cos(2\alpha - \phi) - 9 \cos \phi \right. \\ & \left. + 3\sqrt{3} \sin \phi + 2 \sin \left(\phi - 2\alpha + \frac{\pi}{6} \right) \right], \end{aligned} \quad (34a)$$

$$\begin{aligned} \hat{\mathbf{k}} \cdot \hat{\mathbf{r}}_{13}(t) = & -\frac{1}{2} \cos \theta \left[\cos \alpha + \sin \left(\alpha + \frac{\pi}{6} \right) \right] \\ & + \frac{\sqrt{3}}{24} \sin \theta \left[2 \cos(2\alpha - \phi) - 9 \cos \phi \right. \\ & \left. - 3\sqrt{3} \sin \phi + 2 \sin \left(2\alpha - \phi + \frac{\pi}{6} \right) \right], \end{aligned} \quad (34b)$$

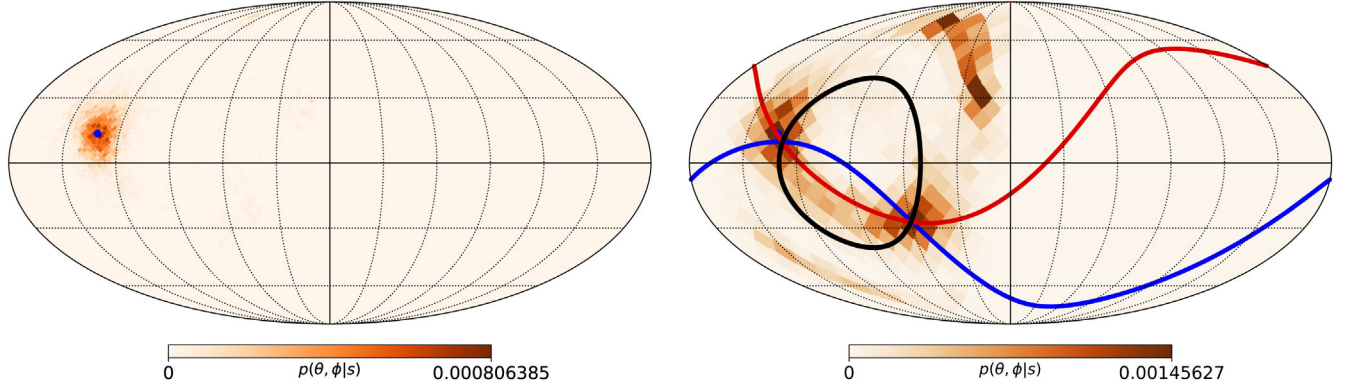


FIG. 5. The joint posterior for the sky location for two bursts of the same central frequency. The burst shown on the left has a short duration ($\tau = 17$ seconds), while the burst shown on the right has a longer duration ($\tau = 2.8$ minutes). The blue dot in the left panel represents the true sky location, which is the same for both sources. Lines of constant projected arm length are shown in the sky map on the right. The blue, red, and black lines are for spacecraft 1 and 2, spacecraft 1 and 3, and spacecraft 2 and 3, respectively. There are two sky locations that satisfy these constraints. There is an additional maxima away from the intersection of these lines that corresponds to a secondary mode with an overall half-period time shift.

$$\hat{\mathbf{k}} \cdot \hat{\mathbf{r}}_{23}(t) = -\frac{\sqrt{3}}{2} \cos \theta \sin \alpha + \sin \theta \left[\sin \left(2\alpha - \phi + \frac{\pi}{6} \right) - 3\sqrt{3} \sin \phi + \sin \left(2\alpha - \phi - \frac{\pi}{6} \right) \right], \quad (34c)$$

where $\alpha = 2\pi f_m t$. When these values, $\hat{\mathbf{k}} \cdot \hat{\mathbf{r}}_{ij}(t)$ which are present in the phase, are well measured the sky location can be determined. In the right panel of Fig. 5 we see the curves on the sky defined by Eqs. (34a)–(34c). The blue curve defines the sky locations that give the same time delay (and the same projected arm length) along the arm connecting spacecrafts 1 and 2 specified by the true sky location of the injected burst. The red line displays the sky locations that maintain the same time delay between spacecraft 1 and 3 as the true sky location. The black line applies to the arm spanned by spacecraft 2 and 3. We see that these curves intersect at two specific sky locations,

one of which coincides with the true sky location by construction. The other intersection is a second mode that the MCMC explored. There exists one other mode which corresponds with a different central time that also provides a good fit to the data. This secondary mode is shifted by a half period in time from the true value. In addition to the time delays, the sky localization is also impacted by the antenna patterns which change the amplitude of the signal in each channel, but this is a weaker effect.

Last, we will also be concerned with the accuracy of our waveform reconstruction, especially in future work where we will work with signals consisting of a superposition of wavelets. Figure 6 shows an example phasemeter glitch Φ_{12}^{pm} with an SNR of 8, a central frequency of 15 mHz, and a τ of 2 minutes ($Q = 17.0$). The observation period was set to 4.55 hours. The dotted black line denotes the signal corresponding to the injected parameters. The red lines denote waveforms for parameters sampled from the

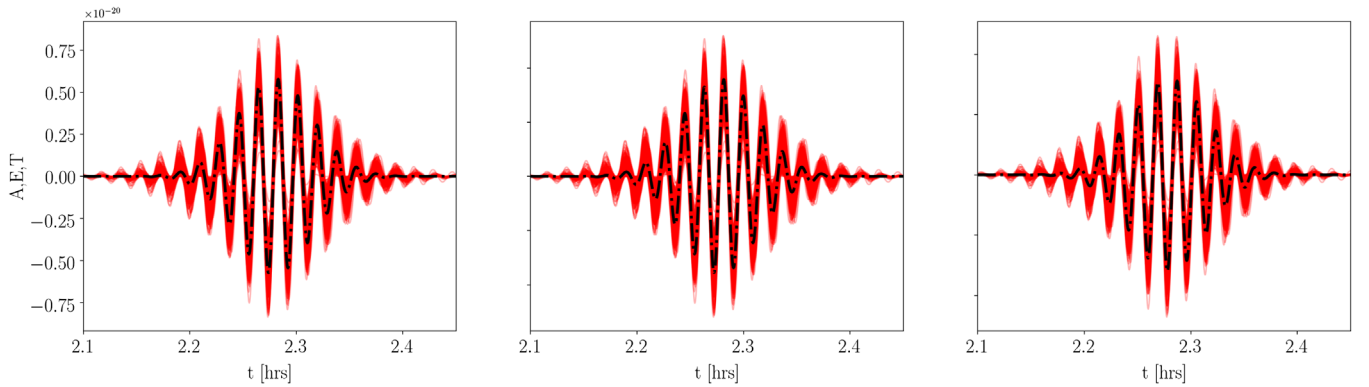


FIG. 6. The left, center, and right panels display the A , E , and T TDI responses respectively for a phasemeter glitch injection denoted by the dot-dashed black line. The red lines are MCMC samples of the waveform. The central frequency for this wavelet is 15 mHz, and $\tau = 2$ minutes.

MCMC. Where the amplitude of the wavelet is largest we see that the MCMC sampled wavelets hug the injected waveform more tightly; the errors in the wavelets are greater near the edges.

V. MODEL SELECTION

Now we will investigate whether we will be confused when identifying whether the data contains a glitch or signal. Recall that glitches enter the data stream with time delays of the arm light travel times. On the other hand, gravitational wave bursts instead enter the data stream with delays equal to the *projected* arm lengths $L(1 - \hat{\mathbf{k}} \cdot \hat{\mathbf{x}}_{ij})$. This impacts the phasing of the response, which can be used to infer the origin of the glitch. This phasing information will be shown to be a more powerful discriminant in higher-frequency glitches. Whether we call a glitch high frequency or low depends on whether the wavelet's central frequency is larger or smaller than LISA's transfer frequency. Additionally, there are important differences between GW bursts and instrument glitches in where they place power in the TDI channels. Gravitational wave signals whose frequencies are below the transfer frequency have a greatly diminished response in the T channel. Additionally, the fact that gravitational waves are seen in at least two TDI channels, while glitches are only seen in one or two channels, will be of great importance. In this section we first demonstrate through a simple argument that we do not expect to confuse GW signals with glitches when all six laser links are operational. Later in this section we will more rigorously demonstrate this conclusion by calculating the Bayesian evidence. We will also study whether it is the phasing of the response or the power distributed in the TDI data channels that provides the greatest leverage for separating GW bursts from instrument glitches.

If one has access to the A , E , and T data channels it is easy to make an argument that we will almost never confuse a glitch for a signal. Consider the following: noise in the data streams will affect our ability to match the true signal. A measurement of this match is the fitting factor (FF), i.e., a normalized (such that 1 indicates a perfect reconstruction of the signal) noise-weighted inner product, between the data and model waveform, maximized over all model parameters. The noise in the data leads to statistical deviations in the fitting factor, even if the true parameters and model are used. The expected deviation from a fitting factor of 1 is described by [19]

$$1 - FF = \frac{D - 1}{2\rho^2}, \quad (35)$$

where D is the dimension of the model.

Let us consider the scenario of an acceleration glitch model, which crops up in the X channel only, when the data actually contains a gravitational wave burst. In the low-frequency limit, where we would expect to be most

confused, the burst does not have significant power in the T channel and also $A \sim h_+$, $E \sim h_\times$. Recall that in the frequency domain $\tilde{h}_\times = i\epsilon\tilde{h}_+$. The overlap (normalized noise-weighted inner product) between the acceleration glitch and burst is

$$\begin{aligned} & \frac{\sum_I (\mathbf{s}_I | \mathbf{h}_I)}{\sqrt{(\sum_I (\mathbf{s}_I | \mathbf{s}_I)) (\sum_J (\mathbf{h}_J | \mathbf{h}_J))}} \\ &= \frac{\frac{2}{3} (\mathbf{A}_B | \mathbf{X}_{ac})}{\rho \sqrt{(\frac{2}{3})^2 (\mathbf{X}_{ac} | \mathbf{X}_{ac}) + (\frac{1}{3})^2 (\mathbf{X}_{ac} | \mathbf{X}_{ac})}}, \end{aligned} \quad (36)$$

where ρ is the SNR of the burst injection. This overlap is maximized if somehow the acceleration glitch conspires to be proportional to the burst's A channel response $\mathbf{X}_{ac} \propto \mathbf{A}_B$. Let us also assume that the A channel response to the burst accounts for a fraction x of the squared SNR, i.e., $(\mathbf{A}_B | \mathbf{A}_B) = x\rho^2$. We then find that the overlap simplifies to $2\sqrt{x}/5$. If in the worst case scenario, all of the burst's SNR is in the A channel the largest fitting factor that can be obtained is 0.89; similar considerations for all other glitches demonstrate that this glitch is indeed the worst case in the regime under consideration.

Should we be concerned by a fitting factor this large? To answer this question we can consider Eq. (35) to understand the statistical error in the fitting factor. Inserting the value 0.89 into this equation results in an SNR of 4.3. We can loosely understand this SNR as the largest SNR possible for the burst that could result in confusion regarding the origin of the data (i.e., whether it was a glitch or signal). So we see that, under some very general assumptions, it is only when a burst is marginally detectable that we might confuse it for an instrument glitch.

A. Bayesian evidence

To more rigorously find out which model best explains the data we must calculate the ratio of evidences $p(\mathbf{s} | \mathcal{M})$ for two given models. This quantity is known as the Bayes factor

$$B_{ij} = \frac{p(\mathbf{s} | \mathcal{M}_i)}{p(\mathbf{s} | \mathcal{M}_j)}. \quad (37)$$

In this subsection we calculate the Bayes factor for competing glitch and burst models for different injections such that we can understand our ability to distinguish a signal's origin and to determine when we cannot. We calculate the Bayes factor via thermodynamic integration [20]. Since we have utilized parallel tempering in our MCMC we can calculate the average log likelihood $E_\beta[\log p(\mathbf{s} | \vec{\lambda}, \mathcal{M})]$ for each temperature of the MCMC by simply calculating the sample mean of the log likelihood values for each sample in the chain. With these in hand one may calculate the evidence for a model via the integral

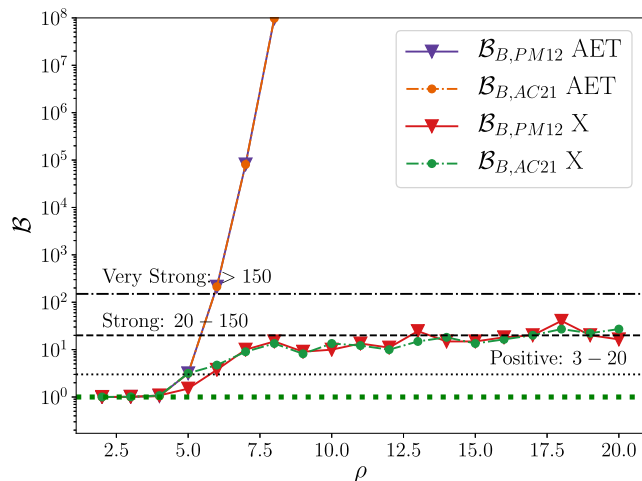


FIG. 7. Bayes factors as functions of the signal-to-noise ratio. A burst was injected into the data stream with a central frequency of 15 mHz and $\tau = 2$ minutes. The purple and orange lines represent the Bayes factor when the A , E , and T TDI channels are used. Note that for the A , E , and T lines the Bayes factors lie on top of each other. The red and green lines represent the case when only the X TDI channel was used. Triangles denote the GW burst Bayes factors vs Φ_{12}^{pm} , while circles represent the GW burst Bayes factors vs Φ_{21}^{ac} . With the A , E , and T channels we swiftly gain confidence regarding the true model as the SNR grows. The growth of the Bayes factor is much slower when only the X channel is available.

$$\ln p(\mathbf{s}|\mathcal{M}) = \int_0^1 d\beta E_\beta [\log p(\mathbf{s}|\vec{\lambda}, \mathcal{M})]. \quad (38)$$

We perform the integral using the methods described in Refs. [7,21]. The covariance matrix between the log-likelihood values for each temperature is estimated and used to define a log likelihood for the integrand of the thermodynamic integration [21]. The integrand is fit by a cubic spline whose control points and locations are marginalized over via a reversible jump MCMC [22]. The MCMC gives us estimates for the evidence integral (upon integrating the cubic spline) and its associated error.

Figure 7 shows the Bayes factor between the glitch and GW burst models for data containing a simulated burst. We use the notation $\mathcal{B}_{A,B} = p(\mathbf{s}|A)/p(\mathbf{s}|B)$ to represent the Bayes factor in the figure's legend. Additionally, the label B is used to denote the burst model. The burst injections have the same values for θ , ϕ , ψ , and ϵ as the burst discussed in Sec. IV. The other important parameters are the central frequency, set to 15 mHz, and τ set to 2 minutes (giving a quality factor of 17.0). The orange and purple lines denote the Bayes factor when the A , E , and T TDI channels are used and the red and green lines show the Bayes factor when only the X channel was used. The lines marked by upside-down triangles represent the model comparison between the burst model and a phasemeter glitch between spacecraft 1 and 2. The lines marked with circles represent

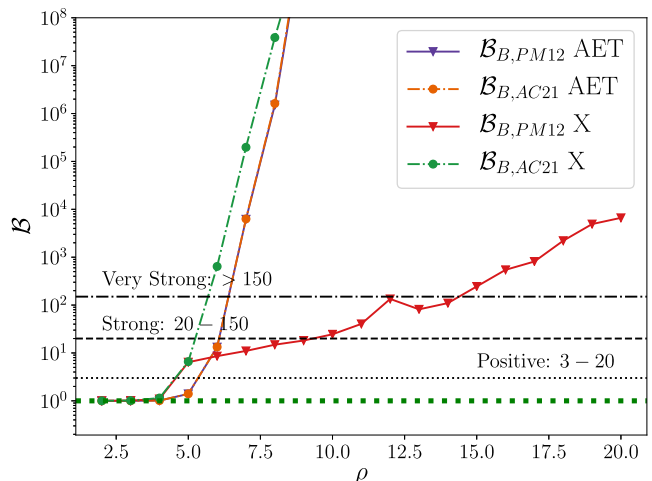


FIG. 8. Bayes factors as functions of the signal-to-noise ratio for a high-frequency burst injection. The lines are labeled according to the same scheme as in Fig. 7. The GW burst is much easier to separate from an instrument glitch in this case.

the Bayes factor between the burst model and an acceleration glitch between the same two spacecraft. The dashed green line represents a Bayes factor of 1, i.e., no preference between the two competing models. A Bayes factor between 3–20 shows positive evidence [23] for the true model. The evidence of the correct model is strong if the Bayes factor lies in the range 20–150, and is considered very strong if the Bayes factor is greater than 150. These regions are denoted by the various dashed horizontal black lines in Figs. 7 and 8. With the A , E , and T channel combination we see that the Bayes factor grows rapidly with the SNR, and for SNRs greater than 5 we are confident that the signal is astrophysical. This supports our argument that GW bursts and glitches are easily separated when we have the full collection of TDI channels. With just the X channel the prospects are not as good, and it is not until the signal reaches an SNR of 10 that it can be confidently distinguished from a glitch. In this low-frequency regime we find that a burst injection recovered with a phasemeter glitch gets a biased central frequency and damping time scale. In Fig. 8 we see the Bayes factors for a high-frequency burst injection, where $f_0 = 50$ mHz and $\tau = 16.9$ seconds ($Q = 5.0$). We see that it is much easier to differentiate a gravitational wave burst from an acceleration glitch. Our ability to distinguish this burst from the phasemeter glitch Φ_{12}^{pm} however is not enhanced as much as that of the acceleration glitch, but it is still improved.

Last, we wish to know how well we can differentiate models for glitch injections. For low-frequency injections the story is similar in that with the full A , E , and T data stream we will be able to differentiate both acceleration and phasemeter glitches through the distribution of power in the different data channels. When we only have the X channel discrimination it once again becomes challenging until the

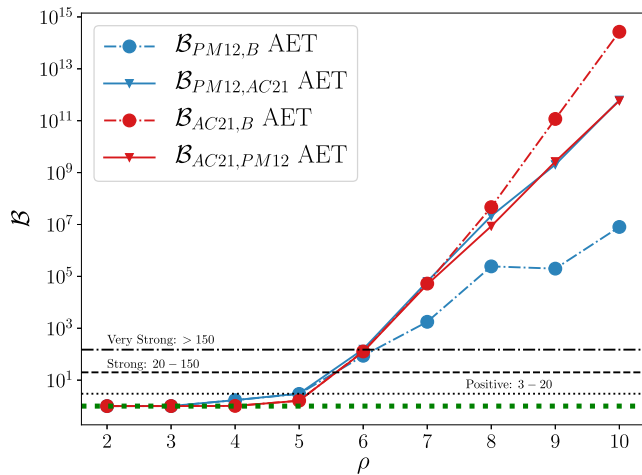


FIG. 9. This figure displays Bayes factors for high-frequency glitch injections. The blue lines denote Bayes factors for a phasemeter glitch Φ_{12}^{pm} injection and the red lines denote a Φ_{21}^{ac} injection.

SNR becomes large. In Fig. 9 Bayes factors are displayed for high-frequency glitch injections. The central frequency of the glitches is 50 mHz and $\tau = 11$ seconds ($Q = 3.5$). The blue lines represent Bayes factors for a phasemeter glitch injection Φ_{12}^{pm} and the red lines represent Bayes factors for an acceleration glitch injection Φ_{21}^{ac} . We see that in this high-frequency regime there will be little issue in discriminating the origin of the signal. This figure also suggests, as seen before, that there might be more of a challenge discriminating this phasemeter glitch from a burst.

VI. DISCUSSION

To realize the full discovery potential of the LISA observatory we need to be in a position to detect unexpected and unknown signals. We have developed a forward model for a wavelet basis to represent instrumental glitches and gravitational wave bursts, as a first step towards this goal. Ideally, to separate unmodeled signals from noise, we would have multiple independent LISA observatories. We have shown that this separation is possible with a single

LISA detector, and even with a single TDI data channel, though the performance is much better when all three TDI channels are available. The properties of the signals and glitches can be recovered with good accuracy, though degeneracies in some parameters can degrade sky localization.

There are several extensions that will need to be made to handle generic glitches and signals. In our analysis we assumed that the Gaussian noise levels were both equal and known. In reality the power spectral density of the noise in each component will have to be estimated from the data, as was done in Refs. [11,12]. We will also need to generalize the analysis to model nonstationary noise, a complication we know LISA will experience owed at least in part to the significant contribution to the noise by unresolved galactic binaries [14]. Our analysis in this paper took a quasi-Bayesian approach via the maximization of the likelihood over extrinsic parameters through the \mathcal{F} -statistic. In the future a full marginalization will have to be done, though the \mathcal{F} -statistic could be used to produced very effective proposal distributions for the MCMC based on maps of the \mathcal{F} -statistic likelihood.

For gravitational wave bursts we will generalize the polarizations to not be elliptically polarized. One last crucial extension is the use of multiple wavelets in the analysis [7]. Not only will we need to characterize multiple wavelets, but we will also need to marginalize over the number of wavelets in the data stream. Due to the shear number of combinations of wavelets we expect in the data stream we expect that the implementation of an effective reversible jump MCMC [22] will be necessary to address the issue of determining an appropriate number of wavelets and the evidence that a GW signal or an instrument glitch is present in the data. There may be additional information gathered by LISA in the form of instrument monitors. These could provide crucial information for characterizing glitches and assessing whether a glitch has indeed occurred.

ACKNOWLEDGMENTS

T. R. and N. J. C. appreciate the support of the NASA Grant No. NNX16AB98G.

- [1] B. P. Abbott *et al.* (LIGO Scientific and Virgo Collaborations), *Phys. Rev. Lett.* **116**, 061102 (2016).
- [2] B. P. Abbott *et al.* (LIGO Scientific and Virgo Collaborations), *Phys. Rev. Lett.* **119**, 161101 (2017).
- [3] P. Amaro-Seoane *et al.*, arXiv:1702.00786.
- [4] M. Armano *et al.*, *Phys. Rev. Lett.* **116**, 231101 (2016).
- [5] M. Armano *et al.*, *Phys. Rev. Lett.* **120**, 061101 (2018).

- [6] T. Robson and N. Cornish, *Classical Quantum Gravity* **34**, 244002 (2017).
- [7] N. J. Cornish and T. B. Littenberg, *Classical Quantum Gravity* **32**, 135012 (2015).
- [8] C. Pankow *et al.*, *Phys. Rev. D* **98**, 084016 (2018).
- [9] M. Tinto, F. B. Estabrook, and J. W. Armstrong, *Phys. Rev. D* **65**, 082003 (2002).

-
- [10] L. J. Rubbo, N. J. Cornish, and O. Poujade, *Phys. Rev. D* **69**, 082003 (2004).
- [11] M. R. Adams and N. J. Cornish, *Phys. Rev. D* **82**, 022002 (2010).
- [12] M. R. Adams and N. J. Cornish, *Phys. Rev. D* **89**, 022001 (2014).
- [13] N. Cornish and T. Robson, [arXiv:1803.01944](https://arxiv.org/abs/1803.01944).
- [14] N. Cornish and T. Robson, *J. Phys. Conf. Ser.* **840**, 012024 (2017).
- [15] E. Thrane and C. Talbot, [arXiv:1809.02293](https://arxiv.org/abs/1809.02293).
- [16] N. J. Cornish and J. Crowder, *Phys. Rev. D* **72**, 043005 (2005).
- [17] C. J. F. T. Braak, *Stat. Comput.* **16**, 239 (2006).
- [18] R. H. Swendsen and J.-S. Wang, *Phys. Rev. Lett.* **57**, 2607 (1986).
- [19] K. Chatziioannou, A. Klein, N. Cornish, and N. Yunes, *Phys. Rev. Lett.* **118**, 051101 (2017).
- [20] T. B. Littenberg and N. J. Cornish, *Phys. Rev. D* **80**, 063007 (2009).
- [21] T. B. Littenberg and N. J. Cornish, *Phys. Rev. D* **91**, 084034 (2015).
- [22] P. J. Green, *Biometrika* **82**, 711 (1995).
- [23] J. D. Romano and N. J. Cornish, *Living Rev. Relativity* **20**, 2 (2017).